Downhole Microseismic Monitoring Using Time-Division Multiplexed Fiber-Optic Accelerometer Array

FEI LIU [1,7], **SHANGRAN XIE** [2], **MIN ZHANG** [3,7], **BIN XIE** [4], **YONG PAN** [4], **XIANGGE HE** [3], **DUO YI** [5], **LIJUAN GU** [3], **YUTING YANG** [6], **ZHANGYUAN CHEN** [7], **(Member, IEEE)**, **HAILONG LU** [3], **AND XIAN ZHOU** [1], **(Member, IEEE)**

[1]Beijing Engineering and Technology Research Center for Convergence Networks and Ubiquitous Services, University of Science and Technology Beijing, Beijing 100083, China
[2]Max Planck Institute for the Science of Light, 91058 Erlangen, Germany
[3]College of Engineering, Peking University, Beijing 100871, China
[4]Petro China Xinjiang Oilfield Company, Karamay 834000, China
[5]College of Physics and Optoelectronic Engineering, Shenzhen University, Shenzhen 518061, China
[6]School of Software and Microelectronics, Peking University, Beijing 100871, China
[7]State Key Laboratory of Advanced Optical Communication Systems and Networks, Peking University, Beijing 100871, China

Corresponding author: Min Zhang (zhang_min@pku.edu.cn)

ABSTRACT Microseismic monitoring is of importance for several geoscience research aspects and for applications in oil and gas industry. For signals generated by the ultra-weak microseismic events, conventional moving-coil geophone systems have reached their limit in detection sensitivity especially at high frequency range. Here we for the first time present a specially tailored fiber-optic sensing system targeting at downhole microseismic monitoring. The system contains 30 individual interferometric accelerometers and 2 reference sensors, which are time-division multiplexed into a 12-level vector seismic sensor array. The multiplexed accelerometers can achieve $\sim$50 ng/$\sqrt{Hz}$ noise equivalent acceleration, which is superior to the commercial available moving-coil geophone systems at frequencies above 200 Hz. The measured sensitivity of the accelerometers can reach $\sim$200 rad/g from 10 Hz to 1 kHz. The dynamic range is above 134 dB over the same frequency range and is higher than its electronic counterpart in the low frequency band. Moreover, the sensors can function properly under the harsh condition of 120 °C temperature and 40 MPa pressure over the 4-hour test duration. The sensor array along with the interrogator has been running uninterruptedly over 3 weeks in a multi-stage hydraulic fracturing stimulation field test. On-site results show that our system can clearly resolve the vector nature of both compressional and shear waves generated by the microseismic events.

INDEX TERMS Fiber-optic accelerometer, seismic sensor, time-division multiplexing, microseismic monitoring.

I. INTRODUCTION

Microseismic monitoring has demonstrated as an efficient tool for both geophysical investigations and energy industry. Initially applied in geothermal energy exploration and exploitation [1], it has been widely used to characterize physical processes related to fluid injection and extractions [2], block caving for mining [3] and hydraulic fracturing especially for unconventional oil and gas production [4].

The associate editor coordinating the review of this manuscript and approving it for publication was Leo Spiekman.

In laboratory, A. L. Turquet *et al.* detected microseismic signals to study the localization of the acoustic emission source with the aim of understanding fluid-induced earthquake nucleation process [5]. By dealing with microseismic point clouds, i.e. cluster of the interpreted microseismic events, McKean *et al.* proposed a probabilistic method for fracture network identification [6].

To observe microseismic events, downhole monitoring systems (rather than surface or near-surface ones) are normally preferred due to their relative higher signal to noise ratio (SNR) and broader detection bandwidth [7]–[9]. The

downhole seismic systems are expected to have a low noise equivalent acceleration (NEA) of some 10 ng/$\sqrt{Hz}$ along with a dynamic range larger than 120 dB [10]. Specifically, the NEA level is required to be low enough especially at higher frequencies in order to capture the ultra-weak microseismic events. At the same time the dynamic range needs to be large enough at low frequency range to avoid signal distortion since it is known that stronger microseismic events generally feature a stronger low frequency components [11]. Moreover the sensors are required to survive in harsh environments [12] since they need to be deployed in borehole close to the seismic source to minimize signal attenuation and ambient noise [8]. As a promising alternative technique to conventional moving-coil geophone systems, fiber-optic seismic sensors have attracted great attentions over the last two decades owing to their high sensitivity, broad detection band, electric-free nature and the capacity of large-scale multiplexing [13]. Permanent downhole fiber-optic seismic systems with their active seismic field tests have been reported by BP Inc. [13]. Optoplan AS Company has developed a high-resolution fiber-optic sensor for downhole imaging, the detection bandwidth and NEA of which ranges from 10 Hz to 800 Hz and 100 to 500 ng/$\sqrt{Hz}$ respectively [14]. Paulsson *et al.* proposed a borehole seismic vector sensor using fiber Bragg gratings and has demonstrated 55 dB SNR in a laboratory test [12]. Recently, their optimized system has also been applied to geothermal reservoir imaging and monitoring [15]. Till now, all previous work focused on active seismic applications such as vertical seismic profiling rather than microseismic monitoring. In the latter case, a much lower noise level at higher frequencies (>500 Hz) as well as a long-term stability are required [16]. Furthermore, on-site results of downhole microseismic monitoring using fiber-optic-sensor-based systems have not yet been reported.

In this work, we for the first time report a microseismic sensing system based on interferometric accelerometers and present its on-site downhole monitoring results. A compliant-cylinder-type fiber-optic accelerometer was used as the unit of seismic transducer. All sensors (in total 32 pieces) were time-division multiplexed sharing one laser source. Results show that the developed fiber sensor array can provide a lower NEA level compared to moving-coil geophone systems at high frequencies as well as an increased dynamic range for the low-frequency band. These characteristics specifically make the system favorable for microseismic events detection. The principle and detailed design of the sensor unit and the multiplexed array are firstly introduced in the paper, followed by the experimental results in both laboratory and downhole environments.

II. PRINCIPLE OF THE FIBER-OPTIC SEISMIC SENSOR UNIT

A. THE SEISMIC SENSOR UNIT

Fig. 1(a) illustrates the mechanical structure of the proposed fiber-optic accelerometer. A compliant cylinder made of soft flexible material (poly sulfone) and the inertial mass
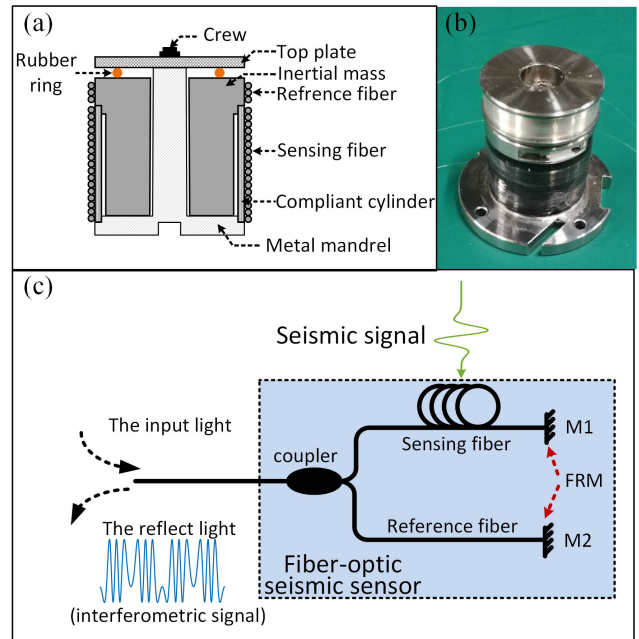
FIGURE 1. (a) The mechanical structure and (b) the photograph of the seismic sensor unit. (c) The optical beam path of the interferometric accelerometer.

(stainless steel), both supported by a mental mandrel (stainless steel), form a mass-spring system. The crew, top plate and rubber ring fix the inertial mass on the metal mandrel. The sensing fiber is wrapped around the cylinder under an appropriate tension while the reference fiber winding around the inertial mass. Fig. 1(b) is the photograph of one piece of the fabricated sensing unit using the mechanical structure shown in Fig. 1(a).

When external seismic signal induces acceleration ($a(t)$) onto the sensor unit, the mandrel moves upwards causing the inertial mass to push downwards against the cylinder. The compressed cylinder then transfers this relative movement to a phase change of the optical beam propagating in the sensing fiber due to the change of fiber length as well as the elasto-optical effect [17]. While the optical phase of the beam propagating along the reference fiber remains unchanged since the Young's modulus of the inertial mass is extremely large (∼200 GPa). The difference in phase change between sensing and reference arms is converted to the intensity change (i.e. the interferometric signal) via using an unbalanced fiber-optic Michelson interferometer (with path length difference between two arms ΔL) as shown in Fig. 1(c). The coupler and Faraday-rotation mirrors (FRMs) were placed at the bottom side of the mandrel (not shown in Fig. 1(a) and (b)). FRMs were coated at the endface of sensing and reference fibers to eliminate the polarization fading effect [18]. The interferometric signal I can be written as [19]:

$$I(t) = I_0 \{1 + \upsilon cos[\varphi_s(t) + \varphi_0]\} \qquad (1)$$

where I_0 is the average light intensity, υ is the visibility, $\varphi_s(t)$ is the phase variation proportional to the applied acceleration

$a(t)$, i.e. $\varphi_s(t) = Ka(t)$. Here K is the sensitivity in unit of rad/g. φ_0 is the initial phase of the interferometer that can be considered as a constant. The phase variation $\varphi_s(t)$ was extracted by the heterodyne interrogation method (see Section II-B).

In this system, the sensitivity K depends on the seismic signal frequency f and the natural frequency f_0 of the sensor unit. Following a Lorentzian lineshape, K can be described as:

$$K(f) = K_0 \frac{f_0^2}{\left[(f^2 - f_0^2)^2 + 4\xi^2 f^2 f_0^2\right]^{1/2}} \quad (2)$$

where

$$f_0 = \frac{1}{2\pi} \left(\frac{k_{eff}}{m + m_{cyl}/3}\right)^{1/2} \quad (3)$$

and ξ is the damping ratio. K_0 denotes the sensitivity at frequencies well below f_0:

$$K_0 = \frac{8\pi^2 nbN\sigma}{\lambda XHK_{eff}}\left(m + \frac{m_{cyl}}{3}\right)$$
$$\times \left\{1 - \frac{1}{2}n^2[(1 - \sigma_f)p_{12} - \sigma_f p_{11}]\right\} \quad (4)$$

where

$$X = 1 - \frac{k_{fn}N}{HEb}[\frac{b^2}{b^2 - a^2}(2\sigma^2 - 1) - \frac{b^2}{b^2 - a^2} + \sigma]$$
$$K_{eff} = \frac{E}{H}\pi(b^2 - a^2) + \frac{2\pi\sigma^2 k_{fn}Nb}{H^2 X} \quad (5)$$

Here $k_{fn} = E_f S_f$ is the normalized fiber stiffness. The derivation of (2) to (5) was conducted in the manner reported in ref [20].

Tab. 1 lists the values of the parameters used in (2) to (5). Given the preferable phase noise floor of $10\ \mu rad/\sqrt{Hz}$, a sensitivity of 40 to 60 dB ref rad/g is required to achieve a NEA level (ratio of phase noise floor and sensitivity) in the range of 10 to 100 $ng/\sqrt{Hz}$ [21]. On the other hand, the natural frequency is preferred higher than 1 kHz to offset from the normal frequency band of microseismic events [9]. According to (3) and (4), both K_0 and f_0 strongly depend on Young's modulus E of the compliant cylinder. Given the accessible material of the compliant cylinder to survive in high temperature ($>100°C$) for a long time, the natural frequency f_0 is set as 1.6 kHz, resulting a designed sensitivity of $\sim$43 dB.

B. THE INTERROGATOR

The interrogator extracts the phase variation induced in the seismic sensor unit. It includes a heterodyne pulse generator and the corresponding demodulation algorithm. Fig. 2(a) shows the setup to generate heterodyne pulse pairs probing the seismic sensor unit. A CW laser at 1550 nm wavelength with low relative intensity noise (<-100 dBc at peak) and phase noise ($<0.4\ \mu rad/\sqrt{Hz}$ at 10 kHz, 1 m optical path) was used as the light source. The beam was then split by a

TABLE 1. List of symbols and their values in Eq. (2)~(5).

| Category	Symbol	Representation	Value
Compliant cylinder	a	Inner radius	15.5 mm
	b	Outer radius	16.5 mm
	σ	Poisson ratio	0.37
	E	Young's modulus	2.6 GPa
	H	Height	24 mm
	m_{cyl}	Mass	3.52 g
Fiber	n	Refractive index	1.465
	σ_f	Poisson ratio	0.17
	λ	Wavelength	1550 nm
	p_{11}	Pockels coefficients	0.121
	p_{12}	Pockels coefficients	0.27
	N	Number of the fiber turns around the cylinder	193
	E_f	Young's modulus	73 GPa
	S_f	Cross-section area	$5.03 \times 10^{-9} m^2$
Inertial mass	m	Mass	116 g
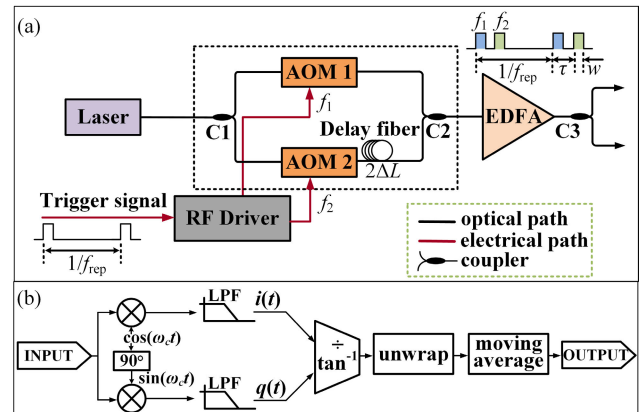
FIGURE 2. (a) The heterodyne pulse generator. AOM, acousto-optic modulator; EDFA, Erbium-doped fiber amplifier. (b) The flow chart of the optical phase variation demodulation algorithm.

50:50 coupler (C1) with each arm applying an acousto-optic modulators (AOM) to generate pulsed light with duration $w = 140$ ns. At the same time the frequency of the two pulses were shifted respectively by f_1 and f_2. Another 50:50 coupler (C2) combines those frequency-shifted pulses, with one of them passing through a delay fiber (length of $2\Delta L = 40$ m). In this way a pulse pair separated by the time interval τ can be generated. The relation between τ, w and ΔL is given by:

$$\tau = \frac{2n\Delta L}{c}$$
$$w \le \tau \quad (6)$$

where c is the speed of light in vacuum therefore $\tau = 200$ ns. The AOMs were trigged at a repetitive frequency $f_{rep} = 200$ kHz. An Erbium-doped fiber amplifier (EDFA)

was added after C2 to compensate the fiber loss. The amplified pulse light was split by C3 for two groups of sensors as introduced in Section III.

Since the optical path difference of the unbalanced Michelson interferometer (i.e. the accelerometer), was set as ΔL (20 m, i.e. half-length of the delay fiber in the pulse generator), as shown in Fig. 1(c), the former pulse (with shifted frequency f_1, the blue one in Fig. 2(a)) reflected by mirror M1 is able to overlap with the latter one (with shifted frequency f_2, the green one in Fig. 2(a)) reflected by mirror M2, generating a pulsed interferometric signal with the heterodyne frequency of $f_c = |f_1 - f_2| = 50$ kHz.

The pulsed interferometric signal reflected back from the sensor was acquired by a photodiode and was then digitized by an analog-digital converter. Similar to the previously reported procedures [22], the interferometric signal was firstly mixed with the orthogonal components of the heterodyne carrier (Fig. 2b). The mixed signal then passed identical low-pass filter (LPF) with an impulse response function $h(t)$, yielding $i(t) = Bsin(\varphi_s(t) + \varphi_0)$ and $q(t) = Bcos(\varphi_s(t) + \varphi_0)$ (note B depends on I_0, υ, and $h(t)$). Finally, $\varphi_s(t)$ can be retrieved by a digital arctangent operation and unwrapping, followed by moving average to remove φ_0. The demodulation algorithm was implemented on a field programmable gate array (FPGA) chip to guarantee a high speed, real-time and multi-channel parallel signal processing.
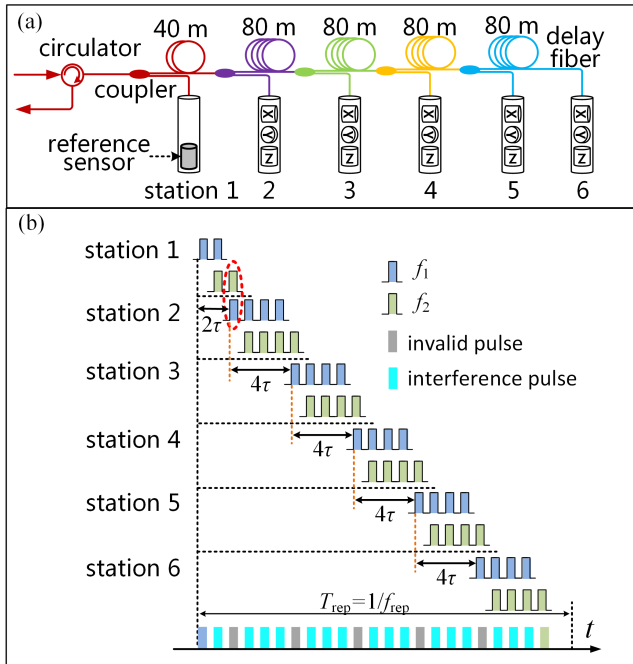
III. THE SENSOR STATION AND SENSOR ARRAY

Three sensor units were orthogonally stacked composing a 3-component (3C) vector sensor station to unambitiously pick up the compressional (P) and shear (S) waves in space. This is important to accurately locate the underground microseismic event [21]. Three identical sensor units were time-division multiplexed via an in-line Michelson structure [23] as illustrated in Fig. 3(a). In this configuration, the optical path difference of each accelerometer was set equal to ΔL, ensuring the separation between the reflected pulsed interferometric signal from each sensor in the time domain as illustrated in Fig. 3(b). The splitting ratios of the coupler in X, Y and Z accelerometers were set as ∼1:3, 1:2 and 1:1 respectively to allow approximate equal power levels of the returned pulses from different accelerometers. When deployed in the borehole, the sensor station was tightly pushed against the casing tube by enabling an arm anchoring mechanism to ensure sufficient coupling with the rock formation. The 3C sensor station and the anchoring mechanism were assembled together forming a sensor pod as shown in Fig. 3(c). The influence of the resonant frequency of the sensor pod on the response of the sensor array will be investigated in the future work.

The entire downhole sensor array consists of 12 sensor pods, namely 12 levels, divided into two identical groups. Fig. 4(a) shows the configuration of the first group in which the first level (station 1) was replaced by a reference sensor for common-mode noise suppression [22]. Adjacent sensor stations were combined by a series of fiber couplers,
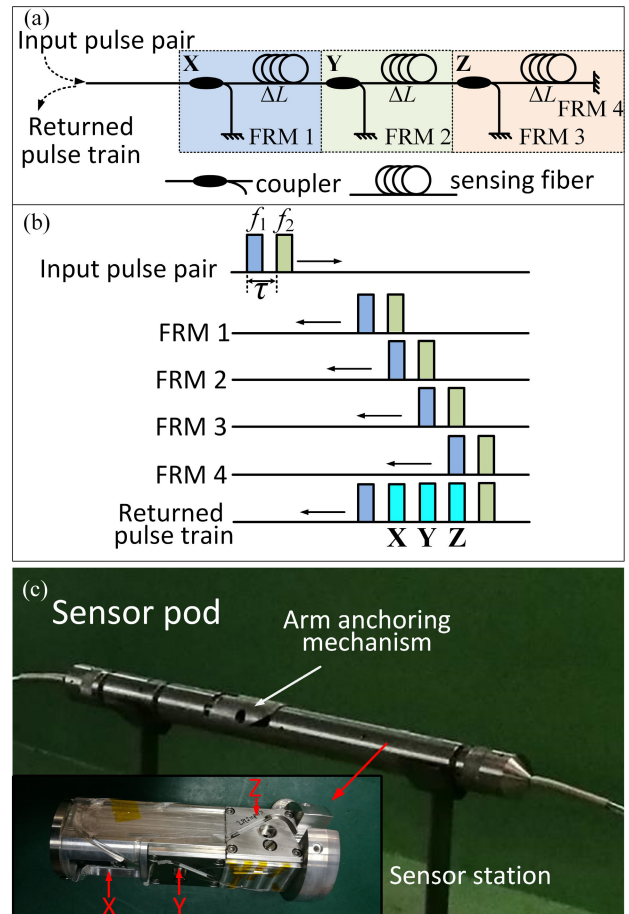

FIGURE 3. (a) The optical beam line of a 3C sensor station. (b) Illustration of the returned pulse train from a 3C sensor station; (c) The photograph of a sensor pod and the contained sensor station. Inset: zoom-in of the sensor station.

the splitting ratio of which were about $N : M$, where N is the number of FRM in the corresponding sensor station and M is the total number of FRM after the coupler. In order to separate the reflected pulse train from adjacent sensor stations in time domain, the delay time between adjacent stations was set as 4τ except the one between station 2 and 1 (which is 2τ). The resultant returned pulse train from the first sensor group is illustrated in Fig. 4(b), showing 16 interferometric pulses representing 16 sensor units (5-level 3C sensor stations plus 1 reference sensor) in the group. It can be seen that in our scheme, the last pulse in the Nth sensor station overlaps with the first pulse from the $(N + 1)^{th}$ station (indicated by the red dashed circle in Fig. 4(b) as one example). The resulting interferometric pulse however barely carry the seismic information since it denotes the interference between pulses returned from adjacent stations rather than the same one. Those "invalid pulse" are represented by the gray rectangles at the bottom of Fig. 4(b). This scheme enables an maximized multiplexing capacity in the system. The second group is the duplication of the first one using another pair of fiber. Once multiplexed, all the 32 sensors (2 groups) in the array can be simultaneously demodulated by the interrogator.

FIGURE 4. (a) Sketch of the time-division multiplexed sensor array containing 6 stations (marked by number below) and (b) the returned pulse train from the array.
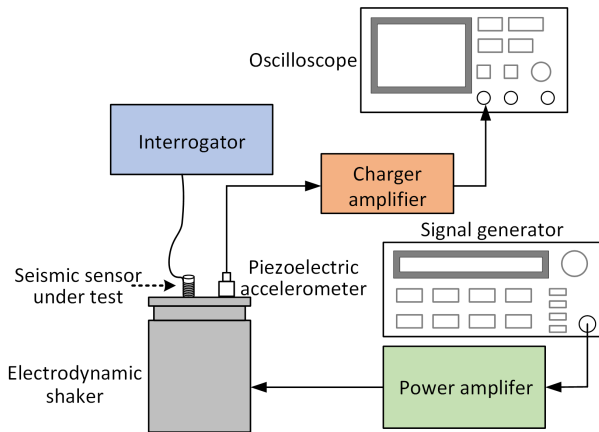

FIGURE 5. Setup to calibrate the sensitivity of the seismic sensor.

IV. SENSOR PERFORMANCE IN LABORATORY ENVIRONMENT

A. SENSITIVITY

The sensitivities of all fiber-optic seismic sensor units were measured by the setup shown in Fig. 5. The vibration was generated by an electrodynamic shaker (ET139, Labworks Inc.) driven by a power amplifier (PA141, Labworks Inc.) which amplifies the sinusoidal electrical signal from a signal generator. The acceleration sensitivity value was calibrated using a piezoelectric accelerometer (LC0401, Lance Inc.), the output of which was amplified by a charger amplifier and was read by an oscilloscope.

The results of the measured sensitivities for all 30 accelerometers versus frequency are summarized
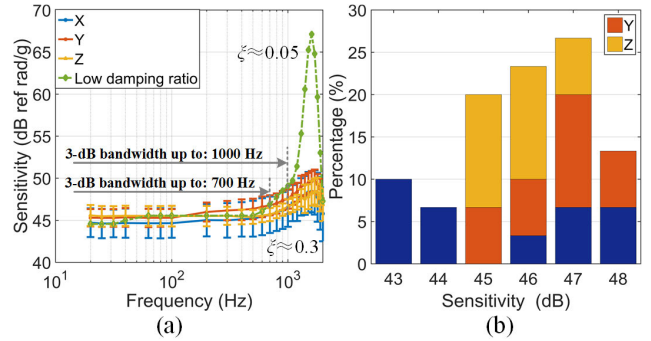
FIGURE 6. (a) The measured averaged values (dots) and the standard deviations (error bars) of the sensitivity over frequency. The green-dashed line is the result from sensor with a low damping ratio. (b) Distribution of the measured averaged sensitivity.

in Fig. 6(a). The blue, red and yellow curves represent respectively the averaged sensitivities of seismic sensors in X, Y and Z directions, with the error bars indicating the corresponding standard deviation. Data below 20 Hz frequency was not available due to the limited frequency band of the shaker as well as the relatively high ambient noise. It is worth noting that in our system the damping ratio ξ of the sensor was optimized to ~0.3 via a proper injection of silicone oil and rubber ring adjustment [24], [25]. This helps in the suppression of the amplitude around the natural frequency (~1.6 kHz) from ~67 dB to ~50 dB compared to the result of non-optimized case (with a damping ratio ξ of ~0.05) which is shown as the green-dashed curve in Fig. 6(a). More importantly, this optimization extends the high-frequency end of the 3-dB bandwidth from 700 Hz to 1000 Hz, which is significant for microseismic event detection since this frequency range contains considerable spectral components according to the collected signal in the field test.

Fig. 6(b) plots the distribution of the averaged sensitivities within the 3-dB bandwidth (20 Hz to 1000 Hz) for all the sensor units. It can be seen that the measured values of sensitivity concentrate ~46 dB (200 rad/g), which is ~3 dB higher than the designed value (43 dB). The discrepancy may be caused by the use of protection glue to fix the wrapped fiber, which degrades the effective Young's modulus of the compliant cylinder. The observed fluctuation in averaged sensitivity (~6 dB) is attributed to the manufacturing tolerant in the fabrication process. Note that the effect of the sensitivity fluctuation on the retrieved phase signal can be mitigated via a proper normalization during signal processing.

B. NEA AND DYNAMIC RANGE

The NEA value (i.e. the minimum detectable acceleration) is defined as:

$$NEA = \frac{NF}{K} \qquad (7)$$

where NF is the noise floor of the retrieved phase variation. This value is expected to at the orders of a few tens of $ng/\sqrt{Hz}$ for downhole applications [10], corresponding to a noise floor lower than -94 dB ref $rad/\sqrt{Hz}$ for a sensitivity of 46 dB.

For each individual accelerometer, a noise floor of -101 dB can be achieved thanks to the effect of common-mode noise suppression [22] and the optimization of the RF driver [26]. The black curve in Fig. 7(a) plots the measured power spectrum density (PSD) for typical non-multiplexed accelerometers. After time-division multiplexing, the measured average noise floor in X, Y and Z directions are shown respectively by the blue, red and yellow curve in Fig. 7(a). The slight deterioration among different directions may be caused by the power imbalance introduced by additional loss including fiber-optic fusion loss and bending loss. The observed higher noise level for less than 100 Hz frequency range is induced by the ambient vibration noise and low frequency temperature drift [27]. The peaks at 50 Hz and its harmonics are caused by electrical noise [27]. A comparison with the non-multiplexed one indicates that multiplexing barely affects the noise level.

The blue-solid curve in Fig. 7(b) plots the retrieved NEA value along with its standard deviation (shaded area) for the fiber sensor array using the measured noise floor and sensitivities. Note the sensitivity values below 20 Hz were considered as the same as that of 20 Hz since $K(f) \approx K_0$ when $f \ll f_0$ (see (2)). It can be seen that the NEA spectrum is quite flat and with a level $\sim 50\ ng/\sqrt{Hz}$. As a comparison, the NEA curves of Slimhole system [28], one of the most widely used commercial downhole seismic system from Geo Space Inc. based on conventional moving-coil geophone (OMNI-2400 from Geo Space Inc. [29]), are also shown as the dashed lines (colors indicating cases with different values of pre-amplifier gain). Since the sampling interval of Slimhole system is 2 ms, its highest frequency limits at 250 Hz. It can be seen that with frequency increasing, the NEAs of Slimhole system firstly reach its minimum value round natural frequency (15 Hz) and then increase, while for the fiber-optic seismic sensor the NEA keeps almost the same. Furthermore, at frequencies above 200 Hz, the NEA of the fiber seismic sensor is expected to be lower than that of Slimhole system regardless the pre-amplifier gain, meaning that the fiber-optic seismic sensor is more suitable to detect high-frequency weak microseismic events.

The dynamic range of the sensor is defined as the ratio between the maximum and minimum detectable signal amplitude. In downhole seismic detection, a dynamic range larger than 120 dB (exceeding six orders of magnitude) is necessary [10], [27]. The minimum detectable signal can be regarded as the noise floor while the maximum detectable signal can be estimated f_c/f_m [21], where f_m is the signal frequency. The measured frequency dependent dynamic range of the multiplexed fiber-optic accelerometer is plotted as the blue-solid curve in Fig. 7(c), along with the comparison with that of Slimhole system. It can be seen that the dynamic range for the fiber system is larger than 134 dB from 10 Hz to 1 kHz. Moreover, the dynamic range is found increased at lower frequencies, which is favorable for downhole applications since seismic signal suffers less absorption by the reservoir at lower frequencies [11]. The dynamic range can be further extended
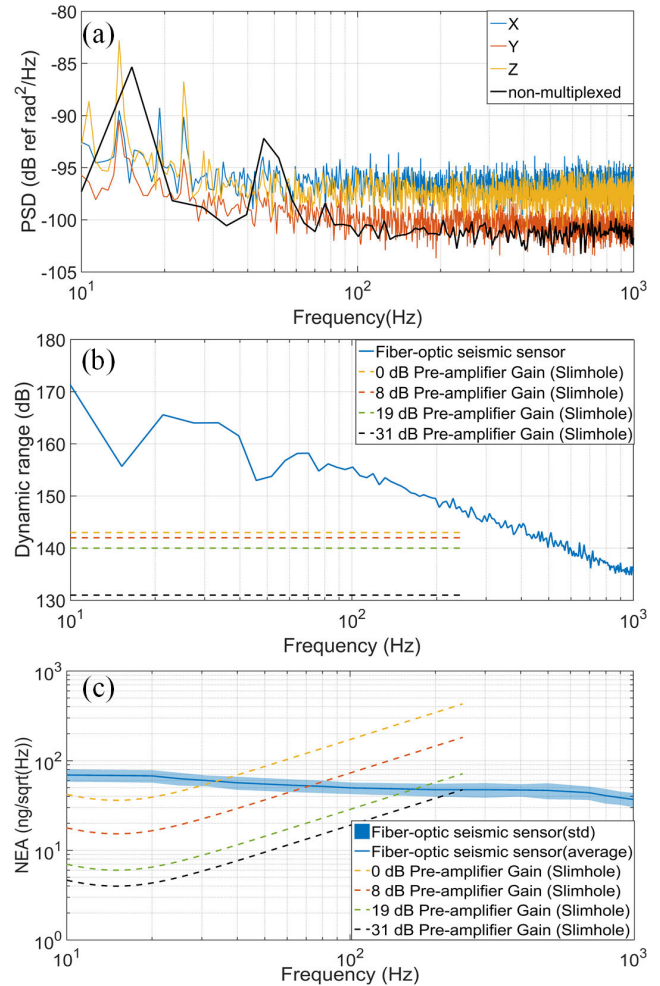

FIGURE 7. (a) Measured averaged noise spectrum in X (blue), Y (red) and Z (yellow) direction of multiplexed seismic sensors. The black curve is the result from non-multiplexed sensor. (b) Measured averaged NEA spectrum (solid line) and its standard deviation (shaded area) of the fiber-optic seismic sensor and the curves for moving-coil geophone system Slimhole with different pre-amplifier gain level (dashed lines). (c) The dynamic range of the fiber-optic seismic sensor and the curves for moving-coil geophone system Slimhole with different pre-amplifier gain level (dashed lines).

by increasing the heterodyne frequency f_c in the interrogator (currently limited by the repetition frequency f_{rep}).

C. CROSSTALK

Several sources contribute to the crosstalk among sensor units once multiplexed, including axis misalignment in the fabrication procedure [21], [27], imperfection of the wavelength-related devices [30], [31], finite extinction ratio of the pulse [32] and the acquisition circuit [33]. A crosstalk value lower than -40 dB is favorable for downhole applications [27]. In the test, the X-direction seismic sensor in level 2 was replaced with a lead-zirconate titanate (PZT) ring applying a sinusoidal strain signal at frequency 315 Hz on the sensing fiber. This method allows to impose signals with high amplitude and to characterize the optical crosstalk among axes and between adjacent stations. The measured
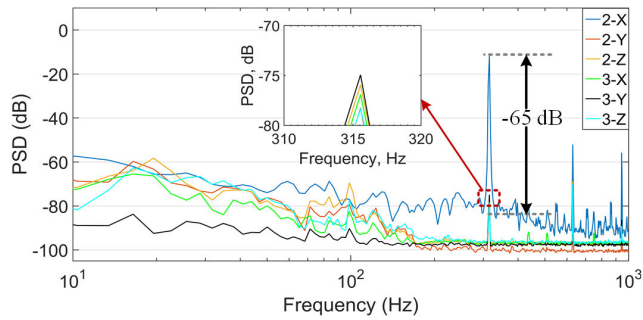
FIGURE 8. The measured crosstalk between sensors within axes in one station and between adjacent stations.
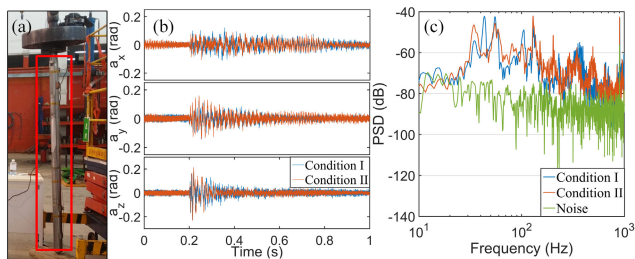

FIGURE 9. (a) Photograph of the sensor pod under test. (b) The recorded acceleration waveform under Condition I (120 °C temperature, 40 MPa pressure, blue curve) and II (room temperature and atmospheric pressure collected after 4-hour continuously running under Condition I, red curve). (c) The averaged PSD curves measured under Condition I (blue) and II (red). The green curve is the noise spectrum.

PSD curves (averaged over 1 hour) of the demodulated signal in X, Y and Z direction in level 2 and 3 of the sensor array are compared in Fig. 8. The crosstalk can be estimated as the difference in peak height between 2-X and other channels at the driving frequency (315 Hz) whose peaks are zoomed in the inset. It can be seen that the crosstalk between the axis and between adjacent stations are both ∼−65 dB. This value is ∼18 dB lower than the previously reported system using wavelength-domain multiplexing technique [30]. In our system, the crosstalk shall be dominated by the axis misalignment when the 3C sensor station is formed [21], which is unfortunately not measured due to the lack of testing apparatus.

D. TEST RESULTS UNDER HIGH TEMPERATURE AND HIGH PRESSURE CONDITIONS

The high temperature and high pressure test was performed in a simulation well in Xinjiang Oilfield Company. The sensor pod under test was marked as the red rectangle in Fig. 9(a). The simulation well can vary environmental temperature from room temperature (20 °C) up to 120 °C and pressure from 10 MPa to 40 MPa. The vibration signal was generated by dropping a weight (∼5 kg) at a fixed height of 1 m and at a location ∼10 m away from the simulation well. The blue curve in Fig. 9(b) shows the recorded signal in X, Y and Z direction under the condition of 120 °C temperature and 40 MPa pressure (condition I), while the red curve represents
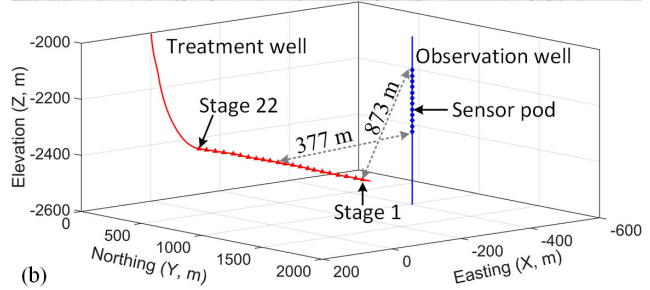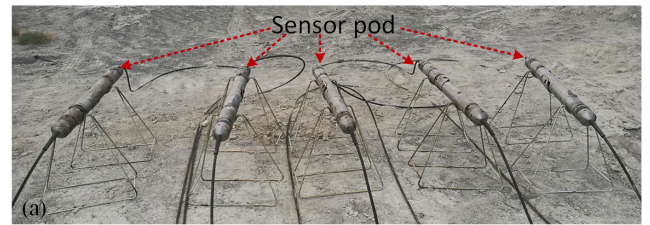

FIGURE 10. (a) The sensor array arranged in the field. (b) Perspective view of the treatment and observation wells in the field test. The origin point was set at the position of the treatment well on the ground.

the result under room temperature and atmospheric pressure (condition II) collected after 4-hour continuously running under Condition I. Fig. 9(c) compares the corresponding averaged PSD curves in both conditions. It can be seen that both curves overlap nicely with each other in the considered frequency range without visible degradations, demonstrating that the sensor pod can survive under the high temperature and high pressure conditions. The green curve in Fig. 9(c) plots the recorded noise level in the test, which is ∼20 dB higher than that in Fig. 7(a) due to the relatively high ambient noise. Despite this a ∼26 dB SNR for the vibration signals was achieved.

V. FIELD-TEST RESULTS

A. SYSTEM DEPLOYMENT

In this section field-test results are presented to demonstrate the system capability on downhole microseismic signal detection. The experiment was conducted in October, 2019, during which the system was running over 3 weeks uninterruptedly. Fig. 10(a) shows part of the arranged sensor array in the field. The sensor array was deployed downhole to a specific depth in the observation well and then clamped against the casing tube with arm anchoring mechanism. The well trajectory of the horizontal treatment well (red line) and observation well (blue line) is depicted in Fig. 10(b). The triangles on the red line (in total 22 stages) mark the locations of fracturing fluid injection points in the horizontal zone at the depth of ∼2376 m. The diamonds on the blue line mark the positions of sensor pods (12 levels) from a depth of 2120 m to 2340 m with a separation between adjacent pod of 20 m. The maximum distance between the sensor pod and the fracturing fluid injection point is 873 m (sensor pod level 1 to stage 1) while the minimum is 377 m (sensor pod level 12 to stage 12). The sensor array continuously captures the vibration signal during the reservoir fracturing process.
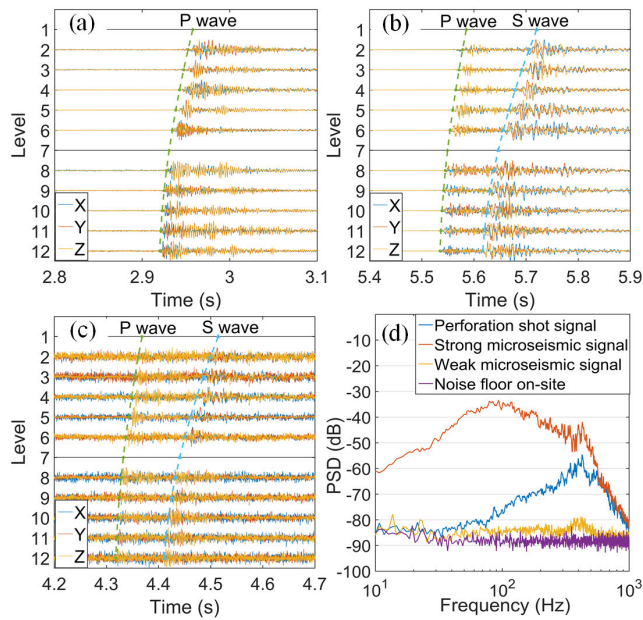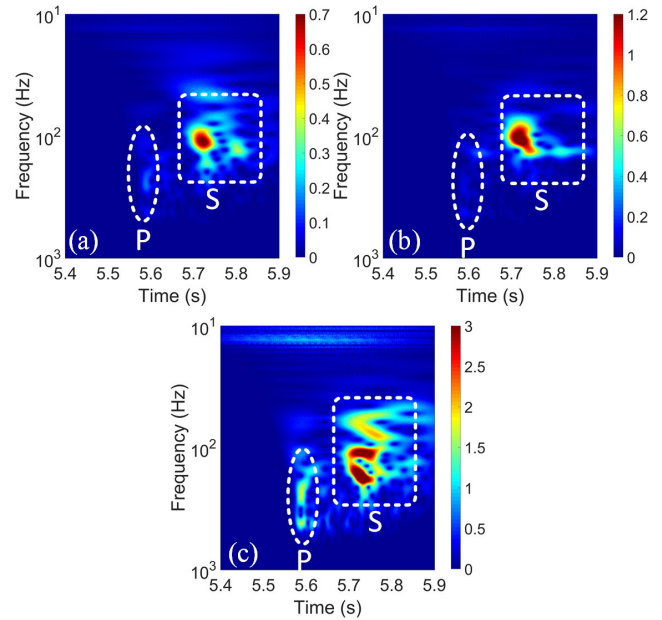
FIGURE 11. The time-domain waveform collected in the field test for (a) the perforation shot signal; (b) relatively strong microseismic event and (c) relatively weak microseismic event. (d) The averaged PSD curves of the signals shown in (a), (b) and (c) as well as the comparison with the noise floor on-site (purple curve).

FIGURE 12. The spectrograms of the (a) X, (b) Y and (c) Z component of microseismic signal collected in level 2 of the sensor array for the relatively strong microseismic signal shown in Fig. 11(b).

B. THE PERFORATION SHOT SIGNAL AND MICROSEISMIC SIGNAL

Fig. 11(a) shows the collected perforation shot signal generated by hydraulic sand-jetting at stage 12 which can be used to calibrate the background velocity and sensor orientations. The blue, red and yellow solid curves represent respectively the waveforms in X, Y and Z direction. It can be seen that the perforation shot signal here barely has *S* wave component. This is because the hydraulic sand-jetting process mainly induces mechanical longitudinal waves on the rocks with negligible shear deformations. Fig. 11(b) and 11(c) displays respectively typical microseismic signals with relatively strong and weak amplitude. The arrival time at all levels was fitted and shown by the green (*P* wave) and cyan dashed curves (*S* wave). It can be seen that in both cases the *P* and *S* waves can be clearly distinguished. The estimated SNR value (using root-mean-square of 1000 data points) for the strong and weak microseismic signal is 43 dB and 3 dB respectively.

Fig. 11(d) compares the PSD curves for the signals in Fig. 11 (a)-(c) as well as the collected on-site noise floor (purple). The noise floor is ~10 dB higher than that in Fig. 7(a) due to the induced noise in the fracturing process. The results reveal that typical microseismic signal occupies a wide frequency band from 10 Hz to 1 kHz and the energy of events with a larger amplitude shifts to lower frequency. This can be explained by their difference in corner frequencies and the dispersive propagation loss [11].

3C vector sensor is able to further reveal the diverse characteristics for *P* and *S* waves generated by the microseismic events. Fig. 12 plots the spectrograms (via wavelet transformation) of the X, Y and Z component in level 2 of the sensor array corresponding to the relatively strong microseismic signal shown in Fig. 11(b). It can be seen that the Z component responds more strongly to *P* wave than other two components while X and Y components have a higher responsivity to *S* wave than *P* wave. Furthermore, it is revealed that the frequency of *P* wave spans from 200 Hz to 500 Hz, while the *S* wave distributes from 50 Hz to 200 Hz. This information helps to improve the location accuracy for the microseismic events [21], [34].

VI. CONCLUSIONS

A specially-designed downhole microseismic monitoring system using fiber-optic accelerometer array is reported. Our results show that via time-division multiplexing and heterodyne demodulation, the system can achieve a NEA value as low as 50 $ng/\sqrt{Hz}$ and a dynamic range higher than 134 dB, which are superior to the commercial available electronic counterparts in certain frequency range. The optical crosstalk between three axes and adjacent stations in the array is measured −65 dB. The low noise level at high frequency band along with the large dynamics range in low frequency band offer an advantageous solution for microseismic detection. Downhole experiments demonstrate that the system can clearly capture the microseismic events and properly resolve the propagation of *P* and *S* waves due to its low noise level, high dynamic range and multi-level feature of the sensor array. The vector nature of the sensor array can assist in disclosing interesting features for *P* and *S* waves. Our results benchmark the state-of-art performance for fiber-optic microseismic sensing system, facilitating the great potential on its future application in gas and oil industry.

REFERENCES

[1] J. N. Albright and C. F. Pearson, "Acoustic emissions as a tool for hydraulic fracture location: Experience at the fenton hill hot dry rock site," *Soc. Petroleum Eng. J.*, vol. 22, no. 4, pp. 523–530, Aug. 1982.

[2] S. A. Shapiro, C. Dinske, and E. Rothert, "Hydraulic-fracturing controlled dynamics of microseismic clouds," *Geophys. Res. Lett.*, vol. 33, no. 14, pp. 1–5, 2006.

[3] M. R. Hudyma, "Analysis and interpretation of clusters of seismic events in mines," Ph.D. dissertation, Dept. Civil Resour. Eng., Univ. Western Australia, Crawley, WA, Australia, 2008.

[4] S. Maxwell, D. Chorney, and M. Grob, "Differentiating wet and dry microseismic events induced during hydraulic fracturing," in *Proc. 3rd Unconventional Resour. Technol. Conf.*, Society of Exploration Geophysicists, American Association of Petroleum, 2015, pp. 1–12.

[5] A. L. Turquet, R. Toussaint, F. K. Eriksen, G. Daniel, O. Lengliné, E. G. Flekkøy, and K. J. Måløy, "Source localization of microseismic emissions during pneumatic fracturing," *Geophys. Res. Lett.*, vol. 46, no. 7, pp. 3726–3733, Apr. 2019.

[6] S. H. McKean, J. A. Priest, J. Dettmer, and D. W. Eaton, "Quantifying fracture networks inferred from microseismic point clouds by a Gaussian mixture model with physical constraints," *Geophys. Res. Lett.*, vol. 46, no. 20, pp. 11008–11017, Oct. 2019.

[7] L. Eisner, M. P. Thornton, and J. Griffin, "Challenges for microseismic monitoring," SEG Tech. Program Expanded Abstr., SEG Annu. Meeting, San Antonio, TX, USA, Tech. Rep. 30-1, 2011.

[8] S. C. Maxwell, J. Rutledge, R. Jones, and M. Fehler, "Petroleum reservoir characterization using downhole microseismic monitoring," *Geophysics*, vol. 75, no. 5, pp. 75A129–75A137, Sep. 2010.

[9] D. Eaton, M. van der Baan, J.-B. Tary, B. Birkelo, N. Spriggs, S. Cutten, and K. Pike, "Broadband microseismic observations from a montney hydraulic fracture treatment, Northeastern BC, Canada," *CSEG Recorder*, vol. 1150, no. 1200, p. 1250, 2013.

[10] P. J. Nash, G. A. Cranch, and D. J. Hill, "Large-scale multiplexed fiber optic arrays for geophysical applications," *Proc. SPIE*, vol. 4202, pp. 55–65, Dec. 2000.

[11] L. Eisner, D. Gei, M. Hallo, I. Opršal, and M. Y. Ali, "The peak frequency of direct waves for microseismic events," *Geophysics*, vol. 78, no. 6, pp. A45–A49, Nov. 2013.

[12] B. N. P. Paulsson, J. Thornburg, and R. He, "A fiber optic borehole seismic vector sensor system for high resolution CCUS site characterization and monitoring," *Energy Procedia*, vol. 63, pp. 4323–4338, Jan. 2014.

[13] B. E. Hornby, F. X. Bostick, B. A. Williams, K. A. Lewis, and P. G. Garossino, "Field test of a permanent in-well fiber-optic seismic system," *Geophysics*, vol. 70, no. 4, pp. E11–E19, 2005.

[14] S. Knudsen, G. B. Havsgård, A. Berg, D. Thingbø, F. Bostick, and M. Eriksrud, "High resolution fiber-optic 3-C seismic sensor system for in-well imaging and monitoring applications," in *Proc. Opt. Fiber Sensors*, 2006, p. FB2.

[15] B. Paulsson, M. Wylie, R. He, H. Hardiman, C. Mancia, and D. Patel, "A fiber optic single well seismic system for geothermal reservoir imaging and monitoring," in *Proc. 44th Workshop Geothermal Reservoir Eng.*, 2019, pp. 1–8.

[16] A. Baig and T. Urbancic, "Magnitude determination, event detectability, and assessing the effectiveness of microseismic monitoring programs in petroleum applications," *CSEG Recorder*, vol. 35, no. 2, pp. 22–26, 2010.

[17] C. D. Butter and G. B. Hocker, "Fiber optics strain gauge," *Appl. Opt.*, vol. 17, no. 18, pp. 2867–2869, 1978.

[18] M. Tur, Y. S. Boger, and H. J. Shaw, "Polarization-induced fading in fiber-optic sensor arrays," *J. Lightw. Technol.*, vol. 13, no. 7, pp. 1269–1276, Jul. 1995.

[19] C. K. Kirkendall and A. Dandridge, "Overview of high performance fibre-optic sensing," *J. Phys. D, Appl. Phys.*, vol. 37, no. 18, pp. R197–R216, Sep. 2004.

[20] R. D. Pechstedt and D. A. Jackson, "Design of a compliant-cylinder-type fiber-optic accelerometer: Theory and experiment," *Appl. Opt.*, vol. 34, no. 16, pp. 3009–3017, 1995.

[21] J. M. De Freitas, "Recent developments in seismic seabed oil reservoir monitoring applications using fibre-optic sensing networks," *Meas. Sci. Technol.*, vol. 22, no. 5, May 2011, Art. no. 052001.

[22] F. Liu, S. Xie, X. Qiu, X. Wang, S. Cao, M. Qin, X. He, B. Xie, X. Zheng, and M. Zhang, "Efficient common-mode noise suppression for fiber-optic interferometric sensor using heterodyne demodulation," *J. Lightw. Technol.*, vol. 34, no. 23, pp. 5453–5461, Dec. 1, 2016.

[23] G. A. Cranch, P. J. Nash, and C. K. Kirkendall, "Large-scale remotely interrogated arrays of fiber-optic interferometric sensors for underwater acoustic applications," *IEEE Sensors J.*, vol. 3, no. 1, pp. 19–30, Feb. 2003.

[24] Y. Duo, L. Fei, H. Xiangge, and Z. Min, "Experimental study on transient response of the fiber optic seismic accelerometer," *Opt. Fiber Technol.*, vol. 45, pp. 58–63, Nov. 2018.

[25] Y. Duo, L. Fei, Z. Min, and T. Qingchang, "High-accuracy transient response fiber optic seismic accelerometer using a shock-absorbing ring as a mechanical antiresonator," *Opt. Lett.*, vol. 44, no. 2, pp. 183–186, 2019.

[26] F. Liu, L. Gu, S. Xie, X. He, D. Yi, M. Zhang, and Q. Tao, "Acousto-optic modulation induced noises on heterodyne-interrogated interferometric fiber-optic sensors," *J. Lightw. Technol.*, vol. 36, no. 16, pp. 3465–3471, Aug. 15, 2018.

[27] R. D. Pechstedt and D. A. Jackson, "Performance analysis of a fiber optic accelerometer based on a compliant cylinder design," *Rev. Sci. Instrum.*, vol. 66, no. 1, pp. 207–214, Jan. 1995.

[28] GeospaceTechnologies. *Slimhole Array System*. Accessed: Jan. 1, 2018. [Online]. Available: https://www.geospace.com/wp-content/uploads/2017/12/592-01940-01_D_Brochure-DW150-Slimhole.pdf

[29] GeospaceTechnologies. *Omni-Directional Geophone*. Accessed: Jan. 1, 2018. [Online]. Available: https://www.geospace.com/wp-content/uploads/2018/02/OMNI-2400-Geophone-Brochure.pdf

[30] G. A. Cranch and P. J. Nash, "Large-scale multiplexing of interferometric fiber-optic sensors using TDM and DWDM," *J. Lightw. Technol.*, vol. 19, no. 5, pp. 687–699, May 2001.

[31] H. Xiao, F. Li, and Y. Liu, "Crosstalk analysis of a fiber laser sensor array system based on digital phase-generated carrier scheme," *J. Lightw. Technol.*, vol. 26, no. 10, pp. 1249–1255, May 15, 2008.

[32] S.-C. Huang, S.-W. Lin, M.-H. Chen, S.-C. Hung, and H.-L. Chao, "Crosstalk analysis and system design of time-division multiplexing of polarization-insensitive fiber optic michelson interferometric sensors," *J. Lightw. Technol.*, vol. 14, no. 6, pp. 1488–1500, Jun. 1996.

[33] C. Yang, H.-Y. Zhang, M. Zhang, and Y. B. Liao, "The bandwidth and crosstalk analysis of detection circuit in time-division multiplexing of fiber-optic hydrophone," *Opto-Electron. Eng.*, vol. 37, no. 7, pp. 75–80, 2010.

[34] N. Warpinski, "Microseismic monitoring: Inside and out," *J. Petroleum Technol.*, vol. 61, no. 11, pp. 80–85, Nov. 2009.

FEI LIU was born in Anhui, China, in 1990. He received the B.S. degree from the College of Precision Instrument and Opto-Electronics Engineering, Tianjin University, Tianjin, China, in 2012, and the Ph.D. degree in electronics science and technology from Tsinghua University, Beijing, China, in 2017. He is currently an Assistant Professor with the School of Computer and Communication Engineering and the Engineering and Technology Research Center for Convergence Networks and Ubiquitous Services, University of Science and Technology Beijing. His research interests include interferometric fiber-optic sensors and distributed optical-fibers sensors.

SHANGRAN XIE, photograph and biography not available at the time of publication.

MIN ZHANG, photograph and biography not available at the time of publication.

BIN XIE, photograph and biography not available at the time of publication.

YONG PAN, photograph and biography not available at the time of publication.

XIANGGE HE was born in Henan, China, in 1989. He received the B.S. degree in optoelectronic science and engineering from the Huazhong University of Science and Technology, Wuhan, China, in 2012, and the Ph.D. degree in electronics science and technology from Tsinghua University, Beijing, China, in 2017. He is currently a Research Assistant with the College of Engineering and the Beijing International Center for Gas Hydrate, Peking University, Beijing. His research interest includes distributed optical fiber sensors.

DUO YI was born in Hubei, China, in 1988. He received the B.S. degree in optoelectronic science and engineering from Beijing Jiaotong University, Beijing, China, in 2010, and the Ph.D. degree in materials from the Technology University of Belfort-Montbeliard, Belfort, France, in 2016. He is currently an Assistant Professor with the College of Physics and Optoelectronic Engineering, Shenzhen University, Shenzhen. His research interest includes optical fiber sensors.

LIJUAN GU was born in Puyang, Henan, China, in 1988. She received the B.S. degree in physics from Central China Normal University, Wuhan, China, in 2009, and the Ph.D. degree in optics from Beijing University, Beijing, China, in 2014. She is currently a Research Assistant with the Beijing International Center for Gas Hydrate, Peking University, Beijing. Her research interests include distributed optical fiber sensors and optical scattering using in gas hydrate research.

YUTING YANG was born in Tianmen, Hubei, China, in 1998. She received the B.S. degree from the Wuhan University of Technology, Wuhan, China, in 2019. She is currently pursuing the degree with Peking University, Beijing, China. Her research interest includes optical fiber sensor.

ZHANGYUAN CHEN, photograph and biography not available at the time of publication.

HAILONG LU, photograph and biography not available at the time of publication.

XIAN ZHOU (Member, IEEE) received the Ph.D. degree in electromagnetic field and microwave techniques from the Beijing University of Posts and Telecommunications, China, in 2011. She was a Hong Kong Scholar with the Department of Electrical and Information Engineering, The Hong Kong Polytechnic University, from February 2014 to February 2017. She is currently a Professor with the School of Computer and Communication Engineering, University of Science and Technology Beijing. Her current research interests include optical communication systems, digital signal processing, and distributed optical fiber sensors.

• • •